Secondary Structure Extensions in *Pyrococcus furiosus* Ferredoxin Destabilize the Disulfide Bond Relative to That in Other Hyperthermostable Ferredoxins. Global Consequences for the Disulfide Orientational Heterogeneity†

Peng-Liang Wang,‡ Luigi Calzolai,‡ Kara L. Bren,‡,§ Quincy Teng,‡,|| Francis E. Jenney, Jr.,⊥ Philip S. Brereton,⊥ James B. Howard,# Michael W. W. Adams,⊥ and Gerd N. La Mar*,‡

Department of Chemistry, University of California, Davis, California 95616, Department of Biochemistry and Molecular Biology, Center for Metalloenzyme Studies, University of Georgia, Athens, Georgia 30602, and Department of Biochemistry, University of Minnesota, Minneapolis, Minnesota 55455

Received February 2, 1999; Revised Manuscript Received April 23, 1999

ABSTRACT: The single cubane cluster ferredoxin (Fd) from the hyperthermophilic archaeon *Pyrococcus furiosus* (*Pf*) possesses several unique properties when compared even to Fds from other hyperthermophilic archaea or bacteria. These include an equilibrium molecular heterogeneity, a six- to seven-residue increase in size, an Asp rather than the Cys as one cluster ligand, and a readily reducible disulfide bond. NMR assignments and determination of both secondary structure and tertiary contacts remote from the paramagnetic oxidized cluster of *Pf* 3Fe Fd with an intact disulfide bond reported previously (Teng Q., Zhou, Z. H., Smith, E. T., Busse, S. C., Howard, J. B. Adams, M. W. W., and La Mar, G. (1994) *Biochemistry 33*, 6316−6328) are extended here to the 4Fe oxidized cluster WT (^{1}H and ^{15}N) and D14C (^{1}H only) Fds with an intact disulfide bond and to the 4Fe oxidized WT Fd (^{1}H and ^{15}N) with a cleaved disulfide bond. All forms are shown to possess a long (13-member) α-helix, two β-sheets (one double-, one triple-stranded), and three turns outside the cluster vicinity, each with tertiary contacts among themselves as found in other Fds. While the same secondary structural elements, with similar tertiary contacts, are found in other hyperthermostable Fds, *Pf* Fd has two elements, the long helix and the triple-stranded β-sheet, that exhibit extensions and form multiple tertiary contacts. All *Pf* Fd forms with an intact disulfide bond exhibit a dynamic equilibrium heterogeneity which is shown to modulate a hydrogen-bonding network in the hydrophobic core that radiates from the Cys21−Cys48 disulfide bond and encompasses residues Lys36, Val24, Cys21, and Cys17 and the majority of the long helix. The heterogeneity is attributed to population of the alternate *S* and *R* chiralities of the disulfide bond, each destabilized by steric interactions with the extended α-helix. Comparison of the chemical shifts and their temperature gradients reveals that the molecular structure of the protein with the less stable *R* disulfide resembles that of the Fd with a cleaved disulfide bond. Both cluster architecture (3Fe vs 4Fe) and ligand mutation (Cys for Asp14) leave the disulfide orientational heterogeneity largely unperturbed. It is concluded that the six- to seven-residue extension that results in a longer helix and larger β-sheet in *Pf* Fd, relative to other hyperthermostable Fds, more likely serves to destabilize the disulfide bond, and hence make it more readily reducible, than to significantly increase protein thermostability.

The "bacterial-type" ferredoxins, Fds,[1] are ubiquitous, small electron transfer proteins possessing one or two cubane 4Fe or 3Fe clusters. These proteins, together with the cubane cluster high-potential iron sulfur proteins (Hipips) and "plant type" 2Fe Fds, are currently of significant interest in the context of the control of protein folding on redox potential(s) (for reviews, see *1*−*3*). Such cubane Fds have been isolated from several so-called hyperthermophiles which are microorganisms that thrive optimally at >80 °C. These Fds exhibit significant sequence homology to the considerably less thermostable Fds from mesophiles (see Figure 1A−D). Two of them have been structurally characterized, one from the

† This work was supported by grants from the National Science Foundation (MCB 9600759 to G.N.L. and 9405783 to M.W.W.A.) and the National Institutes of Health (GM45597 to M.W.W.A.).

* Address correspondence to Dr. Gerd N. La Mar, Department of Chemistry, University of California, Davis, One Shields Avenue, Davis, CA 95616-5295. Tel: (530) 752-0958. Fax: (530) 752-8995. E-mail: lamar@indigo.ucdavis.edu.

‡ University of California.

§ Present address: Department of Chemistry, Rochester University, Rochester, NY 14627.

⊥ University of Georgia.

|| Present address: Department of Chemistry, University of Georgia, Athens, GA 30602.

University of Minnesota.

[1] Abbreviations: Fd, ferredoxin; *Pf*, *Pyrococccus furiosus*; *Tm*, *Thermotoga maritima*; *Tl*, *Thermococcus litoralis*; *Dg*, *Desulfovibrio gigas*; *Bt*, *Bacillus thermoproteolyticus*; *Da*, *Desulfovibrio africanus*; NOE, nuclear Overhauser effect; NOESY, two-dimensional nuclear Overhauser spectroscopy; TOCSY, two-dimensional total correlation spectroscopy; ppm, parts per million; NMR, nuclear magnetic resonance; DSS, 2,2-dimethyl-2-silapentane-5-sulfonate.

10.1021/bi990241n CCC: $18.00
Published on Web 06/02/1999

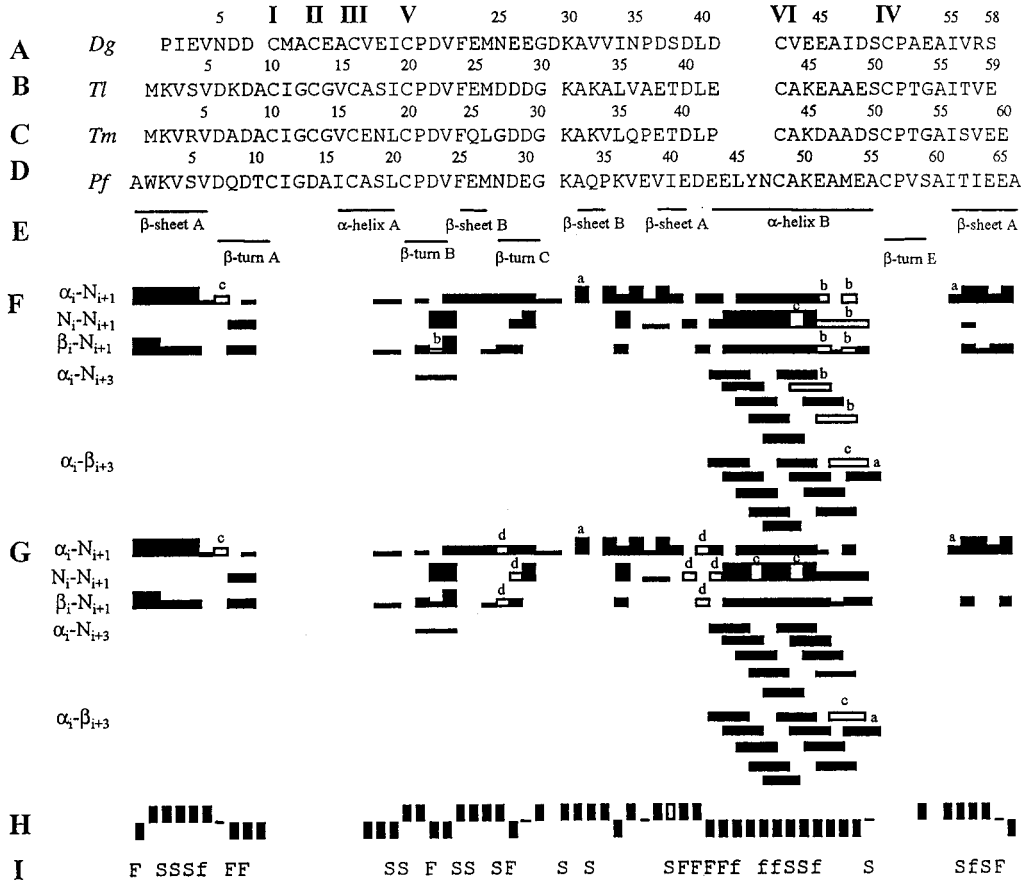

FIGURE 1: Sequence alignment for structurally characterized cubane Fds with disulfide bonds from (A) mesophilic *Desulfovibrio gigas*, *Dg*; (B) hyperthermophilic *Thermococcus litoralis*, *Tl*; (C) hyperthermophilic *Thermotoga maritima*, *Tm*; (D) hyperthermophilic *Pyrococcus furiosus*, *Pf*. The sequences are aligned on the basis of conserved ligands in the cluster consensus ligating sequence, I−IV, the disulfide bond Cys(V) to Cys(VI), and tertiary contacts established herein. (E) Secondary structural elements identified for *Pf* Fd and also observed in the other hyperthermostable Fds (*4*, *6*). The *Dg* Fd has a β-turn in place of the third strand of β-sheet A. Sequential and medium-range NOESY cross-peaks for (F) 4Fe Fd_A^{ox} (with intact disulfide) and (G) 4Fe Fd_B^{ox} (with cleaved disulfide bond): (a) observed only in 50 ms mixing time NOESY spectrum;[3] (b) too broadened by dynamic molecular heterogeneity to detect in Fd_A^{ox}; (c) cross-peak not detected due to near-degeneracy, position under solvent line, or paramagnetic influences; (d) not detected because of exchange effects. (H) The $C_\alpha H$ chemical shift index (*33*) for *Pf* Fd^{ox} (the index is the same for all four forms). (I) Exchange behavior of peptide NHs in 4Fe Fd_A^{ox}, labeled slow (S) when present and intense in ^2H_2O after 24 h, and fast (F, f) when exhibiting saturation transfer above 40 °C (F) and above 70 °C (f).

bacterium *Thermotoga maritima* (*Tm*) 4Fe Fd, both by X-ray crystallography (*4*) and solution NMR (*5*), and one from the archaeon *Thermococcus litoralis* (*Tl*) 4Fe Fd, by solution NMR (*6*). Both possess a highly conserved protein fold and exhibit only the addition of a short third strand to the β-sheet that includes the terminus when compared to the crystal structures for Fds from mesophiles, *Desulfovibrio gigas* (*Dg*) 3Fe Fd (*7*), *Desulfovibrio africanus* (*Da*) 4Fe Fd (*8*), or *Bacillus thermoproteolyticus* (*Bt*) 4Fe Fd (*9*).

The single-cluster Fd from the hyperthermophilic archaeon *Pyrococcus furiosus* (*Pf*) differs from that of other hyperthermostable Fds in both its cluster properties and certain important aspects of its overall folding topology. Thus, the *Pf* Fd cluster possesses an unprecedented Asp14 as cluster ligand II (*10*), exists in a predominant $S = 3/2$ rather than $S = 1/2$ ground state for the reduced state at 4 K (*11*), undergoes facile 3Fe ↔ 4Fe interconversion (*11*), and exhibits a significantly retarded intermolecular electron transfer rate (*12*) when compared to *Tl* Fd (*13*). All of these unusual properties appear to be linked to the cluster-ligating Asp14(II) in *Pf* Fd. On a more global perspective, *Pf* Fd exhibits less sequence homology to other Fds (Figure 1A−D) such as *Tl* and *Tm* Fds, is six (relative to *Tm* Fd) to seven (relative to *Tl* Fd) residues longer than Fds from other hyperthermophiles, possesses a disulfide bond between Cys21(V) and Cys48(VI) (Figure 1D) which, in contrast to the Fds from other hyperthermophiles, is redox active at approximately the same potential as the cluster (*10*, *12*, *15*), and displays structural heterogeneity in all forms with an intact disulfide bond (*10*, *15*−*17*).

Moreover, cycling among the redox states of *Pf* 4Fe Fd with $O_2/S_2O_4^{-2}$ as oxidant/reductant has shown that four distinct redox states are accessible, with oxidized or reduced (superscript ox or red, respectively) clusters and disulfide (subscript A) or free thiols (subscript B) for Cys21(V) and Cys48(VI) (*14*). At 30 °C (some 70 °C below its physiological temperature), the disulfide/free thiol reactivity is so sluggish that not only can the extreme oxidation states Fd_A^{ox} (disulfide) and Fd_B^{red} (free thiol) be prepared in pure form but the two metastable intermediates, Fd_B^{ox} (free Cys) and Fd_A^{red} (disulfide), can also be "trapped" for an extended time as the dominant species in solution. *Pf* Fd thus provides an unparalleled opportunity for structurally characterizing each of the four redox states and learning about the influences of each redox step on the structure. The mechanistic and/or physiological implications of Asp ligation and a redox active

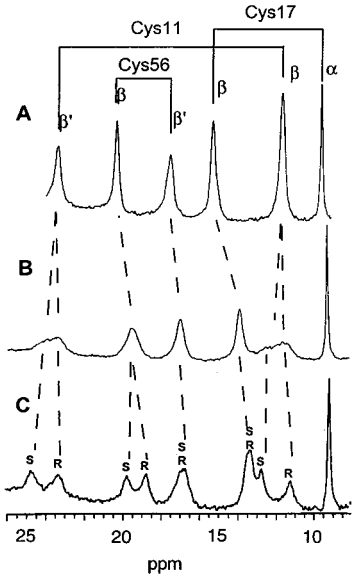

FIGURE 2: Low-field portions of the 500 MHz ^{1}H NMR spectra (*17*) with the assigned Cys ligand $C_\beta H$ resonances of 3Fe Fd_A^{ox} at (A) 50, (B) 20, and (C) 5 °C, showing that two nonequivalent cluster environments can be resolved for these resonances (because of the large chemical shift difference) due to an equilibrium dynamic heterogeneity in the configuration about the Cys21(V) to Cys48(VI) disulfide bond. The split resonances are labeled S or R for the resolved peaks, with "S" and "R" corresponding to the deduced chirality of the disulfide bond for the two "frozen out" forms, respectively (see Discussion).

disulfide are not understood at this time. The relationship between these unusual properties and the structure(s) of the different states, however, provides fertile ground for elucidating the detailed influences of ligand and cluster environment on the electronic structure and redox potential.

In this report we address some of the more global structural properties of *Pf* Fd. Thus, solution ^{1}H NMR spectra of *Pf* Fd_A (intact disulfide) exhibit anomalous line broadening for the resolved, hyperfine shifted cluster ligand peaks (*10*, *14*−*16*), which indicates that the structure is heterogeneous. This heterogeneity is most dramatically illustrated in the effect of temperature on the hyperfine shifted region of the ^{1}H NMR spectra for 3Fe *Pf* Fd^{ox}, as shown in Figure 2 (*16*). The resolution at low temperature of two sets of cluster ligand peaks, differentiated by subscripts *S* and *R* (see Discussion), reveals the presence of two populated, interconverting species which exhibit significant differences in the cluster electronic structure (*16*). The fact that the populations of the two species change with temperature suggests that the structure of this Fd at ambient temperature is different from that at the organism's physiological temperature of over 100 °C. Moreover, *Pf* Fd has failed to yield single crystals suitable for X-ray diffraction, and the structure of the complex resulting from cocrystallization of *Pf* Fd^{ox} with one of its partner oxidoreductases shows its structure, for the most part, is disordered (*18*). This disorder may have the same origin as that detected by ^{1}H NMR. Last, it has been shown that the equilibrium molecular heterogeneity manifests itself in low-temperature broadening of the ^{1}H NMR signals for the ligated Cys in all forms of *Pf* Fd with an intact disulfide (i.e., Fd_A), while similar low-temperature line broadening is absent in all forms with free thiols for Cys21 and Cys48 (i.e., Fd_B) (*10*, *14*, *15*, *19*).

The objective of the research reported here was to define the secondary structure and tertiary contacts remote from the clusters in various forms of *Pf* Fd. In these regions paramagnetic relaxation does not significantly modulate the intensity of the key NOESY cross-peaks needed to qualitatively define structure. We sought to address the following questions: How does the secondary structure and/or tertiary contacts for *Pf* Fd_A^{ox} differ from those of Fds from mesophiles and other hyperthermophiles? What are the structural consequences of abolishing the disulfide link between Cys21 and Cys48? What is the structural basis of the equilibrium molecular heterogeneity of *Pf* Fd_A^{ox} and is it a "local" or "global" phenomenon? How far from the cluster, and in what manner, does the structure of *Pf* Fd respond to perturbations of cluster ligands (Asp14 vs Cys14) and cluster architecture (3Fe vs 4Fe)? What is the structural/functional role of the six or seven additional residues of *Pf* relative to *Tm* and *Tl* Fds? Lastly, does the structure of *Pf* Fd provide insight into why the disulfide bridge is readily reducible by dithionite in *Pf* but not in *Tl* or *Tm* Fd?

MATERIALS AND METHODS

Proteins. Pyrococcus furiosus (DSM 3638) was grown in a 600 L fermenter, and its ferredoxin was purified under reducing conditions (*20*). This yields the protein with a reduced cluster and two free thiols (4Fe Fd_B^{red}). Unless noted otherwise, all procedures were carried out under strictly anaerobic conditions. Samples for NMR spectroscopy were equilibrated with 50 mM sodium phosphate buffer, pH 7.6. Where indicated, samples were exchanged into 95% ^2H_2O/5% ^1H_2O in an Amicon ultrafiltration device utilizing a YM 3 membrane. The two redox states relevant to this work, 4Fe Fd_A^{ox} and 4Fe Fd_B^{ox}, were prepared as described in detail previously (*10*, *14*). 4Fe Fd_B^{ox} (oxidized cluster, $[Fe_4S_4]^{+2}$, free thiols for Cys21, Cys48) was prepared by treating 4Fe Fd_B^{red} with O_2 for 15 min followed by deoxygenation and purging with Ar. 4Fe Fd_A^{ox} (oxidized cluster, $[Fe_4S_4]^{+2}$, disulfide between Cys21, Cys48) was prepared by treating 4Fe Fd_B^{red} with O_2 for 36 h at 30 °C followed by deoxygenation.

For the production of recombinant ^{15}N-labeled Fd in *Escherichia coli*, plasmid pPfRdFd1 was constructed. This also contained the gene encoding rubredoxin from *Pf* (*21*), and this protein was also obtained in the labeled form.[2] All reagents used were of molecular biology grade, and enzymes were obtained from Stratagene (La Jolla, CA). All standard molecular biology techniques were performed as described (*22*). Plasmid pAH1993 expressing the *Pf* Fd encoding gene (*fdx*) was previously described (*23*). Plasmid pPfRd1,[2] which contains the *Pf* rubredoxin encoding gene (*rub*), was cloned in frame at the *Nco*I/*Pst*I sites of the overexpression vector pTrc99a (Amersham Pharmacia Biotech, Arlington Heights, IL). Oligonucleotide primers (5′-AGa cGC TGC AGA GGA AAC AGA CAT ATG GCG TGG AAG GTT TCT GTC-3′ and 5′-AAC TTA AGC TTT CAA GCC TCC TCA ATA GTA A-3′) were utilized in a polymerase chain reaction to generate a product containing the *Pf fdx* gene with a *Pst*I restriction site, as well as a ribosome binding site (AGGA) nine base pairs upstream of the *fdx* gene ATG translation

[2] Jenney, F. E., Jr., and Adams, M. W. W. Unpublished data.

start site at the 5′ end, and a *Hind*III site at the 3′ end for cloning downstream of the *rub* encoding gene on plasmid pPfRd1. The PCR product was gel purified in a 4% agarose gel, and the DNA was isolated using the GeneCleanII kit (Bio101, Vista, CA). Restriction digestion of the PCR product with *Pst*I and *Hind*III was performed under standard conditions as described (*22*) and was ligated to similarly digested plasmid pPfRd1 to generate plasmid pPfRdFd1, which has both the *Pf rub* and *fdx* genes under control of the IPTG inducible *trc* promoter. The plasmid was transformed into *E. coli* strain XL2-Blue (Stratagene) and repurified. The DNA sequence was determined on both strands using the Sanger dideoxy sequencing method with the Sequenase 2.0 sequencing kit (Amersham) to confirm the construction. Plasmid pPfRdFd1 was then transformed into *E. coli* strain NCM533 for overexpression of the two *Pf* proteins.

For recombinant protein expression, *E. coli* NCM533 containing plasmid pPfRdFd1 was grown in a 100 L fermenter at 37 °C stirred at 170 rpm under aerobic conditions in M9 minimal medium (*22*), except that 0.8 g/L $^{15}NH_4Cl$ (>98% ^{15}N, Isotec, Miamisburg, OH) was used instead of the standard 1 g/L NH_4Cl and supplemented with 0.4% glycerol as carbon source, 100 μM $FeSO_4$, 0.05% thiamine, 1x vitamins as described by Venters et al. (*24*), and 100 μg/mL carbenicillin. The culture was then grown to $A_{600} \approx 0.98$, and induced with 1 mM IPTG for 14 h. The purification was performed under anaerobic conditions with all buffers containing sodium dithionite (2 mM). Cells (300 g, wet weight) were lysed using lysozyme (22), incubated at 70 °C for 1 h, and then stored at 4 °C overnight to denature and precipitate *E. coli* proteins. The cellular debris and denatured protein were removed by centrifugation (26000*g*; 45 min). The supernatant was diluted 5-fold with 50 mM Tris-Cl, pH 7.5 (buffer A), and loaded onto a DEAE-Sepharose Fast Flow column (10 × 20 cm) equilibrated with buffer A. The column was washed with buffer A (2 column volumes), and the absorbed proteins were eluted with a two-step linear gradient from 0 to 0.15 M NaCl (one column volume) and from 0.15 to 0.6 M (18 column volumes) in buffer A. The Fd was collected (1.4 L) while between 0.261 and 0.285 M NaCl was applied to the column. The Fd was concentrated by loading it on a Q-Sepharose HP column (2.6 × 6 cm) at a dilution of 25% in 50 mM Tris-Cl, pH 7.5, and eluting with 0.5 M NaCl. A final anion exchange column (Q-Sepharose HP; 6 × 10 cm) was loaded with concentrated Fd at 20% dilution in buffer A and eluted with a gradient from 0 to 0.5 M NaCl (15 column volumes). The Fd was concentrated on a Q-Sepharose column (as described above) and was applied to a column (3.5 × 60 cm) of Sephadex G-75, equilibrated with sodium phosphate (50 mM; pH 7.7) containing 5 mM dithionite at 2.0 mL/min. Fractions containing pure Fd as judged by electrophoretic analysis were combined, concentrated by Q Sephadex chromatography, and stored under N_2.

NMR Spectra. ^1H NMR spectra were recorded at 500 MHz on a GE Omega 500 spectrometer. Chemical shift values were referenced to 2,2-dimethyl-2-sulfonate, DSS. Labile amide protons were detected using the 1:1 "jump and return" pulse sequences (*25*). Two-dimensional ^1H NMR experiments were performed on 5−8 mM samples of Fd prepared in 50 mM phosphate, pH 7.6, H_2O. Data were collected over the temperature range 10−70 °C over a 7017 Hz sweep width, and consisted of 512 t1 blocks each with 96 transients collected over 2048 complex points. Two-dimensional TOCSY (*26*) spectra were collected at a repetition rate of 0.5 s^{-1} and utilized a MLEV 17 spin lock applied for 60 ms. NOESY spectra (*27*) were recorded with 250 ms mixing time and utilized repetition rates of 0.5 s^{-1}. The water signal was suppressed with a low-power selective irradiation during the predelay period for all experiments followed by a SCUBA sequence (*28*) to allow for magnetization recovery of resonances close to the water frequency. Heteronuclear $^{15}N-^1H$ HSQC correlation experiments (*29*) were recorded over the temperature range 10−90 °C using a 4 mM 95% ^{15}N-enriched sample, pH 7.6. Data consisted of 256 t1 blocks each with eight transients collected over 2048 complex points with a repetition rate of 0.5 s^{-1}. NMR data were processed on either a Silicon Graphics Indigo workstation or a SUN Sparc station using the Biosym Felix 2.3 program. For data sets over 7018 Hz sweep width, 30°-shifted sine-bell-squared functions were applied in both dimensions for NOESY and TOCSY, and data sets were zero-filled to 2048 × 2048 real data points prior to Fourier transformation.

RESULTS

The structural studies reported herein focus on thermodynamically and aerobically stable forms of 4Fe *Pf* Fd, (with oxidized cluster and intact disulfide bridge, i.e., 4Fe Fd_A^{ox}) (a form also available with 98% ^{15}N labeling). Sequence specific assignments have already been reported (*17*) for the oxidized 3Fe form (*Pf* 3Fe Fd_A^{ox}), and similar assignments were sought here for 4Fe Fd_A^{ox}, 4Fe D14C-Fd_A^{ox}, and 4Fe Fd_B^{ox} with the reduced disulfide bridge. For the latter metastable complex, all samples contained 10−30% Fd_A^{ox}, and conversion to Fd_A^{ox} in the presence of adventitious oxidant, or disproportionation to Fd_A^{ox} and Fd_B^{red} at elevated temperatures, precluded the collection of useful 2D data above 50 °C. Assignments are described in detail only for Fd_A^{ox} in the sections below.

Sequence Specific Assignments. The assignment of residues experiencing minimal paramagnetic influences was pursued by standard identification (*30*) of the side chain type by 60 ms TOCSY spectra (shown in Figure 3 for 4Fe Fd_A^{ox} and 4Fe Fd_B^{ox}), followed by 250 ms NOESY backbone connectivities as described previously in detail for 3Fe Fd_A^{ox} (*17*), although elevated temperatures (50−60 °C) were necessary to detect the NH−C_αH scalar connectivity for several resonances in all forms except 4Fe Fd_B^{ox} (see below). These methods result in the assignment of backbones for residues 1−10, 19−32, 34−55, and 62−66 and the majority of their side chain protons for each of the Fd forms. The observed sequential α_i-N_{i+1} and N_i-N_{i+1} connections for 4Fe Fd_A^{ox} and 4Fe Fd_B^{ox} are shown in parts F and G of Figure 1, respectively. The assignments for 4Fe Fd_A^{ox} led to corrections in the previous assignments for Ala52 and Ala55 in 3Fe Fd_A^{ox} (*17*). The chemical shifts at 30 °C, pH 7.5, for the assigned residues with minimal paramagnetic influence on spectral properties for each of the four forms are listed in the Supporting Information. Differences in backbone ^1H (and when available, ^{15}N) chemical shifts, using WT 4Fe Fd_A^{ox} as reference (δ(4Fe Fd_A^{ox}) − δ(3Fe Fd_A^{ox}, 4Fe Fd_B^{ox}, or 4Fe D14C Fd_A^{ox})), as a function of sequence position are illustrated graphically in Figure 4.

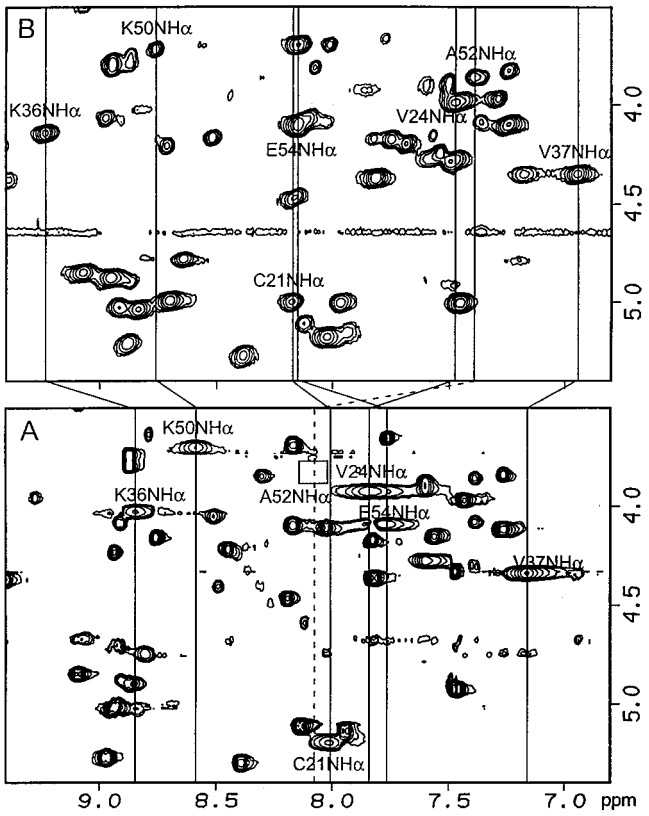

FIGURE 3: Mixing time (60 ms) ^1H TOCSY map in ^1H_2O, pH 7.6, at 30 °C for (A) *Pf* 4Fe Fd_A^{ox} with intact Cys21(V)−Cys48(VI) disulfide bond and (B) ∼75% 4Fe Fd_B^{ox} and ∼25% 4Fe Fd_A^{ox} (with cleaved disulfide). The resonance position of the NHs that exhibit anomalous line broadening in 4Fe Fd_A^{ox} are connected to those in 4Fe Fd_B^{ox} where the line widths are "normal". The dashed line and box in A show where the Ala52 NH shows up at 50 °C.

The sequence specific assignment on the basis of steady-state NOEs of the contact-shifted signals for the cluster ligands, Cys11, Asp14 (or Cys14), Cys17, and Cys56, have been reported for each of the four Fd forms of interest (*10*, *16*, *19*). The residues missing are close to the cluster and hence experience strong paramagnetic relaxation and possible significant hyperfine shifts due to the cluster paramagnetism.[3] In the case of 4Fe Fd_A^{ox}, four additional spin systems could be weakly detected by TOCSY: labeled spin systems A (4.1, 1.3, 0.8 ppm), B (5.20, 2.68, 1.11 ppm), C (4.79, 2.83, 0.93 ppm), and D (4.7, 2.2, 1.8 ppm). For these the NH could not be identified, and they failed to exhibit detectable NOESY cross-peaks to other assigned residues.

Molecular Heterogeneity in the Presence of the Cys21−Cys48 Disulfide Bond. The dynamic molecular heterogeneity, in addition to leading to line broadening (or splitting) for resolved, ligated Cys $C_\beta H$ signals for all Fd_A (as illustrated for 3Fe Fd_A^{ox} in Figure 2), similarly manifests itself in the unresolved peptide NH window of the TOCSY spectrum, as shown in Figure 3A. Anomalously broad ^1H_PN resonances are observed at 30 °C for Cys21, Val24, Lys36, Val37, Lys50, and Glu54 (one additional residue, Ala52, exhibits such ^1H_PN line broadening that it is detectable only at >50 °C). The line broadening is strongly suppressed at elevated temperature and is completely absent in the TOCSY map for 4Fe Fd_B^{ox} (Figure 3B). The degree of this anomalous line broadening of TOCSY cross-peaks for these seven-residue NHs is essentially identical in 3Fe Fd_A^{ox} (*17*), 4Fe Fd_A^{ox}, and 4Fe D14C-Fd_A^{ox} (not shown). The $^1H-^{15}N$ HMQC map of 4Fe Fd_A^{ox} at 20 °C similarly exhibits severely broadened cross-peaks for Cys21, Val24, Lys36, Val37, Lys50, and Glu54 (and Ala52, which is detectable only at >50 °C) which disappear at lower temperature (not shown; see Supporting Information). The HSQC spectra, moreover, reveal that the cross-peaks for Leu45−Ala49, Glu51, Met53, and Ala55 are similarly, but less severely, broadened at 20 °C (not shown; see Supporting Information). As in the case for the ^1H TOCSY spectrum, the anomalous cross-peak broadening in the HMQC spectrum is absent in 4Fe Fd_B^{ox} (not shown; see Supporting Information). The only nonlabile proton to exhibit similarly strongly broadened resonances for each Fd_A^{ox} is one $C_\beta H$ of Cys48(VI) in 4Fe Fd_A^{ox} but not in 4Fe Fd_B^{ox} (see Supporting Information).

The dynamic molecular heterogeneity of Fd_A^{ox} is also shown by the peptide NH temperature gradients (*31*, *32*). A plot of $N_P{}^1H$ shift versus temperature for 4Fe Fd_A^{ox} yields straight lines with slopes near −2 to −8 ppb/°C. This is typically observed for the majority of resonances in folded proteins (*31*, *32*), an example of which is that for Gly31 shown in Figure 5F. The residues which exhibit the anomalous ^1H_PN line broadening, on the other hand, exhibit slopes in the 10−40 °C range that are either positive or much more negative than the majority of other protons, and they show clear changes in the temperature gradient with temperature, as illustrated in Figure 5A−E. Such changes in the gradient are strong support for a dynamic structural heterogeneity (*31*). Curvature in the plot of $N_P{}^1H$ shift versus temperature is only weakly evident for the other N_PHs which exhibit line broadening at low temperature in 4Fe Fd_A^{ox} (not shown). Neither the extreme gradients nor the curvature of the shift versus temperature plot is observed for these resonances in 4Fe Fd_B^{ox} (not shown; see Supporting Information).

Secondary Structure. Essentially the same medium- and long-range NOESY cross-peak patterns were observed for 4Fe Fd_A^{ox}, 4Fe Fd_B^{ox}, and 4Fe D14C−Fd_A^{ox} (although the assignments are less extensive for the latter two complexes). These are the same (although more complete) as those reported for 3Fe Fd_A^{ox} (*17*), showing that all four forms of the protein possess the same secondary structural elements (Figure 1E). Five extended strands involving residues 1−6, 25−27, 33−35, 39−41, and 62−66 (extended to residue 61 by short mixing time 2D data[3]) were identified through strong to moderate α_i-N_{i+1} NOEs in each of the four forms (Figure 1F,G). The two terminal portions and the central residues 39−41 constitute an antiparallel triple strand with the N-terminus at the center. The expected characteristic backbone NOESY pattern shown in Figure 6 gives direct indication for the existence of 10 backbone H-bonds. The expected strong relaxation of the unassigned Ile61 $C_\alpha H$ (estimated $T_1 \sim 50$ ms based on the *Tl* Fd structure (*6*)) and the position of Val6 $C_\alpha H$ close to the solvent line at all temperatures prevented detection of the $\alpha_6-\alpha_{61}$ cross-peak, but the positions of Val6 (and hence Ile61) in the β-sheet are supported by the $C_\alpha H$ shift index for the former residue (*23*). The remaining extended strand pairs in an antiparallel β-sheet B with residues 33−35, although the $\alpha_{33}-N_{34}$ NOE

[3] Calzolai, L., Harklau, H., Bren, K. L., Brereton, P. S., Adams, M. W. W., La Mar, G. N. Manuscript in preparation.

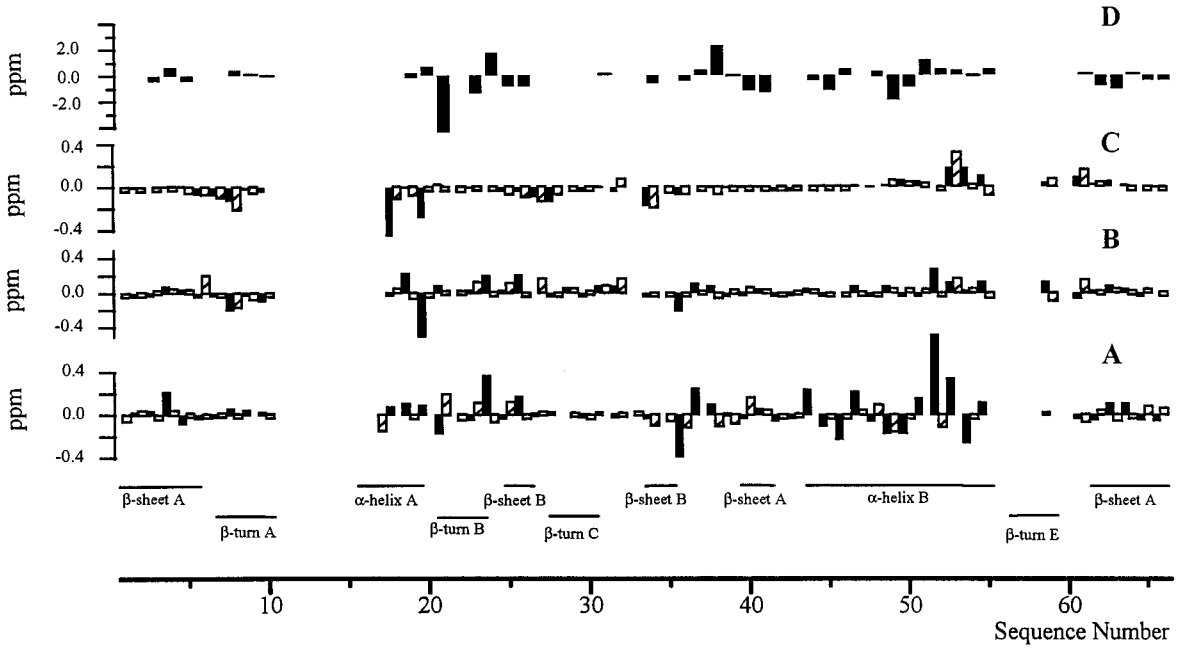

FIGURE 4: Backbone proton chemical shift difference (N_pH closed bars; $C_\alpha H$ open bars) in ppm at 30 °C, among the four complexes of *Pf* Fd using 4Fe Fd_A^{ox} as reference. (A) ^1H δ_{DSS}(4Fe Fd_A^{ox}) − δ_{DSS}(4Fe Fd_B^{ox}), (B) ^1H δ_{DSS}(4Fe Fd_A^{ox}) − δ_{DSS}(3Fe Fd_A^{ox}); (C) ^1H δ(4Fe Fd_A^{ox}) − δ_{DSS}(4Fe D14C Fd_A^{ox}); and (D) ^{15}N δ(4Fe Fd_A^{ox}) − δ(4Fe Fd_B^{ox}). Blanks indicate the assignment is not available in one or the other derivative. The secondary structural element on which a residue resides is shown at the bottom.

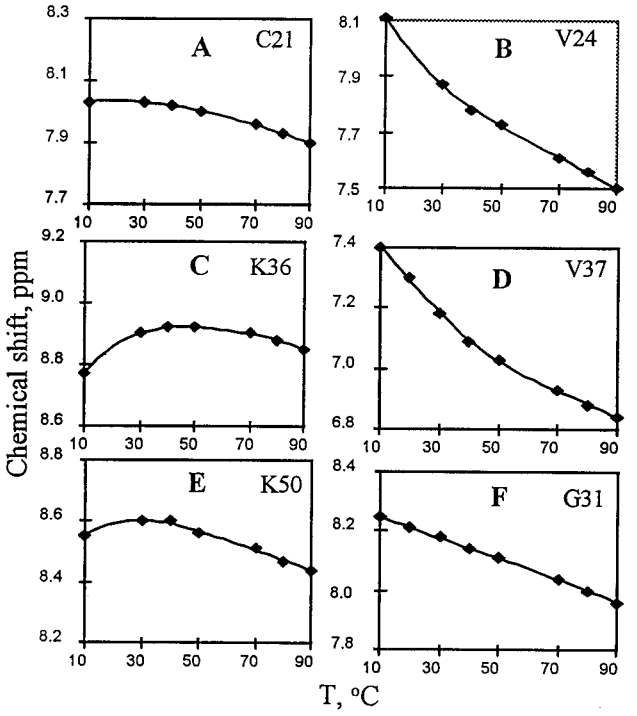

FIGURE 5: Influence of temperature on the peptide proton chemical shift of *Pf* 4Fe Fd_A^{ox} for the anomalously broadened residues: (A) Cys21, (B) Val24, (C) Lys36, (D) Val37, and (E) Lys50, as well as a "normal" residue, (F) Gly 31.

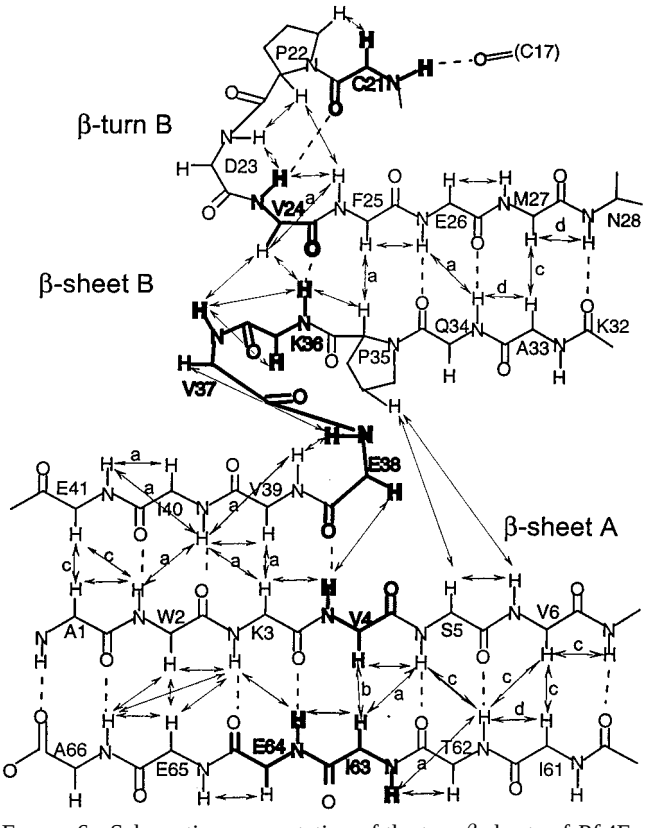

FIGURE 6: Schematic representation of the two β-sheets of *Pf* 4Fe Fd showing observed NOESY cross-peaks (double-sided arrows) and inferred backbone hydrogen bonds (dashed lines): (a) cross-peak is stronger in 4Fe Fd_A^{ox} than in 4Fe Fd_B^{ox}; (b) cross-peak is stronger in 4Fe Fd_B^{ox} than 4Fe Fd_A^{ox}; (c) expected cross-peaks not detected due to near degeneracy, signal under the solvent line, or paramagnetic influences; (d) observed only in a 50 ms mixing time NOESY spectrum.[3]

is not observed and the $\alpha_{23}-N_{28}$ cross-peak is only weak because of relaxation due to proximity to the cluster. The presence of Pro35 in the second strand of β-sheet B likely destabilizes it but appears not to interfere with the Lys36−Val24 H-bond suggested by the NOESY contacts and the slow exchange for Lys37 NH. The characteristic NOEs and implied H-bonds for both β-sheets are given in Figure 6.

The combination of the pattern of N_i-N_{i+1}, α_i-N_{i+1}, β_i-N_{i+1}, α_i-N_{i+3}, and $\alpha_i-\beta_{i+3}$ NOESY cross-peaks (Figures 1F,G) indicates the presence of a 13-member α-helix for residues 43−55 in both 4Fe Fd_A^{ox} and 4Fe Fd_B^{ox}; the

Table 1: Tertiary Contacts between Residues on Identified Secondary Structural Elements in *Pf* 4Fe Fd_A^{ox}

structural elements	residue	residue	structural elements
α-helix B	E43α	W2 ring (m)[a]	β-sheet A
	E43γ[b]	W2 ring (m)	β-sheet A
	Y46 ring[b]	W2 ring (m)	β-sheet A
	Y46 ring[b]	I40γ3 (w), δ (m)	β-sheet A
	Y46 ring[b]	I63γ2 (w), γ3 (s)	β-sheet A
	A49α [A44][c]	[V58] I63δ (w)	β-sheet A
	K50α [K45]	[V58] I63δ (s)	β-sheet A
	M53NH [A48]	[V58] I63δ (m)	β-sheet A
β-sheet A	S5α [R4]	[V34] P35γ (s)	β-sheet B
	V6NH [V5]	[V34] P35γ (w)	β-sheet B
β-turn B	V24γ [V23]	[V3] V4γ (m)	β-sheet A
	V24γ [V23]	[T39] I40β (m), δ (s)	β-sheet A
	V24γ [V23]	[L41] L45β (m), γ (m)	α-helix B
	V24γ [V23]	[A44] A49α (w), β (m)	α-helix B
β-sheet B	F25 ring [F24]	[A44] A49α, β	α-helix B
	F25 ring [F24]	[A47] A52β (m)	α-helix B
	F25 ring [F24]	[I56] I61γ2 (s), γ3 (m)	β-sheet A
	F25 ring [F24]	[V58] I63δ (m)	β-sheet A
	F25 ring [F24]	[C16] C17β (s)	α-helix A

[a] Cross peak intensities, given in parentheses (s, strong; m, moderate; w, weak). [b] Unique in *Pf* Fd due to extension of helix B and β-sheet A. [c] Residues in brackets are equivalent residues in *Tm* Fd (*4*).

expected relaxation effects account for the failure to detect the $\alpha_{54}-N_{55}$ cross-peak since the $^{15}N-^{1}H$ HSQC peak for Ala 55 exhibits "normal" intensity at 30 °C (see Supporting Information). In the case of 4Fe Fd_A^{ox}, the cross-peaks involving the NHs of Ala52 and Glu54 are not detected because of the extensive broadening of these residues by the dynamic heterogeneity (see above). The observed $\alpha_i-\beta_{i+3}$ cross-peaks for $i = 49$ and 51, however, argue for the presence of a 13-member helix in Fd_A^{ox} (spectral congestion precludes the unique detection of the $\alpha_{52}-\beta_{55}$). In the case of 4Fe Fd_B^{ox}, the "normal" narrow line widths for Ala52 and Glu54 N_PHs allow the detection of all connections involving the NHs of the helix (Figure 1G). The presence of the helix in each *Pf* Fd form is supported by the $C_\alpha H$ chemical shift index (Figure 1H). In summary, we observe essentially the same secondary structural elements in all four proteins, with negligible differences among the three Fd_A^{ox} forms and only minor NOESY cross-peak differences between 4Fe Fd_A^{ox} and 4Fe Fd_B^{ox} (see Figures 1 and 6 and Discussion).

Environment of the Disulfide Bond. The close proximity of the two secondary structural elements, turn B and helix B, between which a disulfide bond exists in Fd_A^{ox}, is evident in the NOESY cross-peaks between the $C_\beta Hs$ of Cys21(V) and Cys48(VI) and between Val24 $C_\gamma H_3$ and both the $C_\alpha H$ and $C_\beta H_3$ of Ala49 (see Table 1). These are the expected contacts based on the structures of single-cluster Fds with (*4*, *6*, *7*) or without (*8*, *9*) a disulfide bridge. The largely conserved relationship between turn C and helix B upon cleaving the disulfide to form Fd_B^{ox} is shown by the minimal changes in Val24−Ala45 NOESY cross-peak patterns.

Tertiary Contacts. We restrict ourselves herein to the dipolar contacts among the secondary structural elements remote from the paramagnetic cluster. Contacts between the cluster ligands and the various secondary structural elements in the cluster vicinity, as observed in steady-state NOEs from the $C_\beta Hs$, have been described previously (*19*) for 3Fe Fd_A^{ox}, and they appear to be very similar in 4Fe Fd_A^{ox} (*10*, *15*).

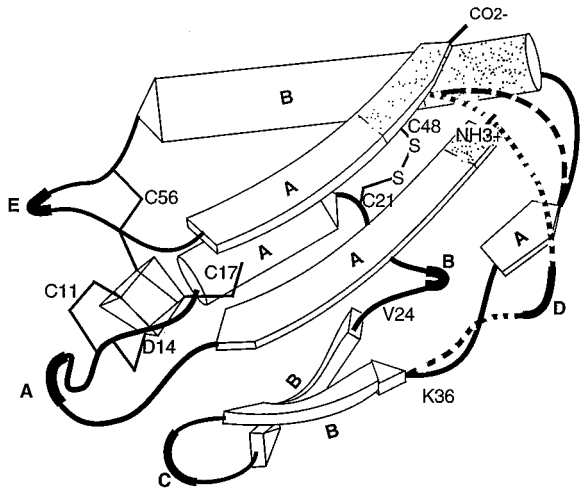

FIGURE 7: Schematic structure of *Pf* Fd generated by simply extending the α-helix B by four residues and β-sheet A by two residues on the N-terminus and by one residue at the C-terminus, relative to the *Tl* Fd structure (*4*). Solid lines illustrate the relative positions of the secondary elements, the cluster, helices A and B, β-sheets A and B, and four β-turns A−D. The position of the disulfide link involving Cys21(V) and Cys48(VI) is also shown. The portion between β-sheet B and helix B retained in the other hyperthermostable *Tm* and *Tl* Fds is shown as a dashed line. The portion of the structure between β-sheet B and helix B retained in the Fd from the *Dg* mesophile is shown as a dotted line. The shaded portion of the structure represents the parallel "modular" extension of helix B and β-sheet A that results from the six or seven extra residues in *Pf* relative to *Tm* or *Tl* Fd.

The observed contacts between pairs of residues on such secondary structural elements are summarized in Table 1. These contacts are the same as those observed for the homologous residues in *Tm* (*4*, *5*) and *Tl* (*6*) 4Fe Fd (for *Tm* Fd given in brackets in Table 1), *but with one very important distinction.* Both β-sheet A and α-helix B are longer in *Pf* Fd than in the Fds from either mesophiles or other hyperthermophiles, and hence contacts between these two secondary structural elements are much more extensive in the *Pf* protein than even those in Fds from other hyperthermophiles. A schematic model that illustrates the unique nature of *Pf* Fd relative to that of other hyperthermophilic and mesophilic Fds is shown in Figure 7.

Labile Proton Exchange. ^{1}H NMR spectra detected with a 1:1 pulse train with and without solvent saturation (not shown; see Supporting Information) show that all peptide NHs not involved in H-bonds within secondary structural elements (either determined here directly, or inferred by the homologous residues in *Tm* or *Tl* Fd), exhibit saturation transfer below 50° and pH 8.6 in both 4Fe Fd_A^{ox} and 4Fe Fd_B^{ox}. At >70 °C, Leu45, Asn47, and Cys48 also exhibited detectable saturation transfer, but to a similar degree in the A and B forms (not shown). Peptide protons whose 2D cross-peaks could be detected 24 h after transfer into $^{2}H_2O$ at pH 7.5 are essentially the same as those reported for 3Fe Fd_A^{ox} (*17*). The NH labilities by residue number are summarized in Figure 1I, using the symbols F (fast, saturation transfer at <50 °C), f (fast, saturation transfer >70 °C), or S (slow, significant intensity in $^{2}H_2O$ 2D map) for the residues whose NHs are assigned. A direct comparison of the exchange behavior of the Ala52 in 4Fe Fd_A^{ox} and 4Fe Fd_B^{ox} was not possible since it required temperatures in excess of 70 °C to reliably detect the cross-peak in the former, while the latter

complex is unstable with respect to oxidation and disproportionation at such temperatures over the time needed to collect comparable data.

DISCUSSION

Structural Comparison to Other Cubane Cluster Fds. All four forms of *Pf* Fd are shown to possess the same secondary structural elements. These include one long helix (B), two β-sheets (one double-stranded (B), one triple-stranded (A)), and three β-turns (A, B, C) (Figure 1E). *Pf* Fd shows the same tertiary contacts among these elements (Table 1) as was previously described for the hyperthermostable *Tl* and *Tm* Fds (*4*−*6*), although expected short helix A and turn E are too close to the cluster to easily characterize by ^{1}H NMR. However, the previously reported NOEs (*10*, *14*, *15*) from Cys17 C_αH to the Leu20 C_βH, from Cys17 C_βH to Phe25 C_βHs, and from Cys56 C_βH to Ser59 C_αH and NH are completely consistent with a highly conserved helix A and turn E in all forms of *Pf* Fd and in *Tl* and *Tm* Fds. The secondary structure of *Pf* Fd differs from that of Fds from mesophiles (*7*−*9*) in the incorporation of a third strand into β-sheet A from the protein interior at the expense of β-turn D in the same manner as observed in *Tl* (*6*) Fd. The qualitative comparison among Fd structures is depicted in Figure 7, where solid lines represent *Pf* Fd. The connection between β-sheet B and helix B in mesophilic Fds is shown by dotted lines, and the connection between the third strand of β-sheet A and helix B for *Tl* and *Tm* Fds is shown in dashed lines.

Simple amino acid sequence alignments with other cubane Fds (Figure 1A−D) suggest that the six- to seven-residue extension in *Pf* Fd compared with structurally characterized and hyperthermostable *Tm* (*4*, *5*) and *Tl* Fds (*6*) appears in the form of a four-residue insertion just prior to Cys48(VI), a one-residue (over *Tl* Fd) or two-residue (over *Tm* Fd) extension of the N-terminus, and a two-residue extension at the C-terminus. Analysis of the tertiary contacts, in fact, confirm completely conserved contacts between residues 3−6 and 61−64 on β-sheet A and residues 48−55 on helix B when compared to the other Fd. Hence, *the additional residues in Pf Fd represent a parallel extension by four residues (*∼*one turn) of helix B and by two residues of* β*-sheet A and in such a manner that these extensions form close contacts*. This "modular extension" of *Pf* over the other Fds is shown by the shaded portion of the model for *Pf* Fd in Figure 7. It is noteworthy that these secondary structural extensions interact strongly via a pair of aromatic residues, Trp2 and Tyr46, not present in other hyperthermostable Fds.

Effect of Cleaving the Disulfide Bond between Cys21 and Cys48. The largely conserved NOESY cross-peak pattern among secondary structural elements upon cleaving the Cys21−Cys48 disulfide bond (compare parts F and G of Figure 1) is consistent with the structures of the crystallographically characterized Fds. These have tertiary contacts between helix A and helix B and are essentially the same in structure near the hydrophobic core whether a disulfide bond is present (as in *Dg* (*7*) or *Tm* (*4*, *5*) Fds) or absent (as in *Da* (*8*) or *Bt* (*9*) Fds). However, the chemical shifts of numerous residues are significantly affected by the disulfide bond change (Figure 4A), and there are two sets of such resonances that merit particular attention. First, there are those (see Figure 4A) exhibited by residues along a well-defined pathway that links Cys21(V) to the cluster and to nearly the extremity of β-sheet A, as shown by the residues in bold in Figure 6. Thus the peptide NHs serve as donors to the carbonyl in the chain Lys36 → Val24 → Cys21(V) → Cys17(III), and the direction of the large NH shift changes upon cleaving the disulfide indicate that the first and third hydrogen bonds are stronger, and the middle weaker, in Fd_B compared to Fd_A. This rearrangement of the hydrogen bond strengths is transmitted to the loop residues, Val37 (strong upfield NH shift) and Glu38 (C_αH shift change). Because of the role of Glu38 as acceptor to the NH of Val4, this leads to a shift change for Val4 and for the paired residues in the other β-strand, Glu64 and Ile63 (Figure 6). The loss of the disulfide bridge also results in an increase in intensity in the $\alpha_4-\alpha_{63}$ NOESY cross-peak and the loss of a weak $N_{62}-N_{63}$ cross-peak, both of which suggest a more regular arrangement of the C- and N-termini strands of β-sheet A in Fd_B than Fd_A. Conversely, loss of the disulfide bond leads to stronger $\alpha_3-\alpha_{39}$ and α_3-N_{40} NOESY cross-peaks, suggesting that the arrangements of the N-terminal and internal strands in β-sheet A are distorted slightly upon cleaving the disulfide.

The other path of significant structural accommodation that occurs upon disulfide cleavage originates at Cys48(VI) and encompasses the majority of helix B, with Lys50, Ala52, and Glu54 NH shifts particularly strongly influenced (see Figure 4A). The difficulty in obtaining direct information on this helical deformation is *that all residues whose NHs are strongly affected by disulfide cleavage also exhibit the severe line broadening in* Fd_A *due to the structural heterogeneity*. Hence many key NOESY cross-peaks for the perturbed residues in all forms of Fd_A are not detectable at temperatures below 60 °C. The high-temperature (T > 70 °C) analysis of NOESY maps, however, was abandoned for the present time because it is expected that *the structural difference between* Fd_A *and* Fd_B *is strongly suppressed at elevated temperature* (see next section).

Structural Basis of the Molecular Heterogeneity of Pf Fd_A^{ox}. That the molecular heterogeneity originates in the vicinity of the disulfide bond is indicated by the fact that it is observed only in *Pf* Fd forms with an intact disulfide bond, that the residues exhibiting the anomalous line broadening form a logical link to Cys21(VI) or Cys48(V), and that a *stable disulfide bond is inconsistent* (see below) *with the qualitative molecular structure of Pf Fd* deduced by analogy to the *Tl* or *Tm* Fds. Disulfide bonds generally adopt either a right- (*S*) or left-handed (*R*) helical orientation (*34*, *35*). In the structurally characterized Fds (*4*, *6*, *7*), the disulfide bond adopts the *S* (right-handed) orientation, as shown in Figure 8A. In these proteins, the alternate *R* orientation is strongly destabilized by steric interaction between the Cys(V) S_γ and the carbonyl oxygen of Cys(VI), as shown in Figure 8B. On the other hand, because of the extension of α-helix B by one turn in *Pf*, the *S* orientation results in severe steric overlap between Cys(VI) S_γ and the carbonyl and C_αH of Leu45 on the helix B extension as well (Figure 8A). The conversion of the *S* disulfide orientation (Figure 8A) to the *R* orientation (Figure 8B) involves 120° rotations of χ_1 for both Cys(V) and Cys(VI) (*34*). The expectation for dipolar contacts in *Pf* Fd for the alternate disulfide orientations can be illustrated by the "generalized" helix B which has been extended by

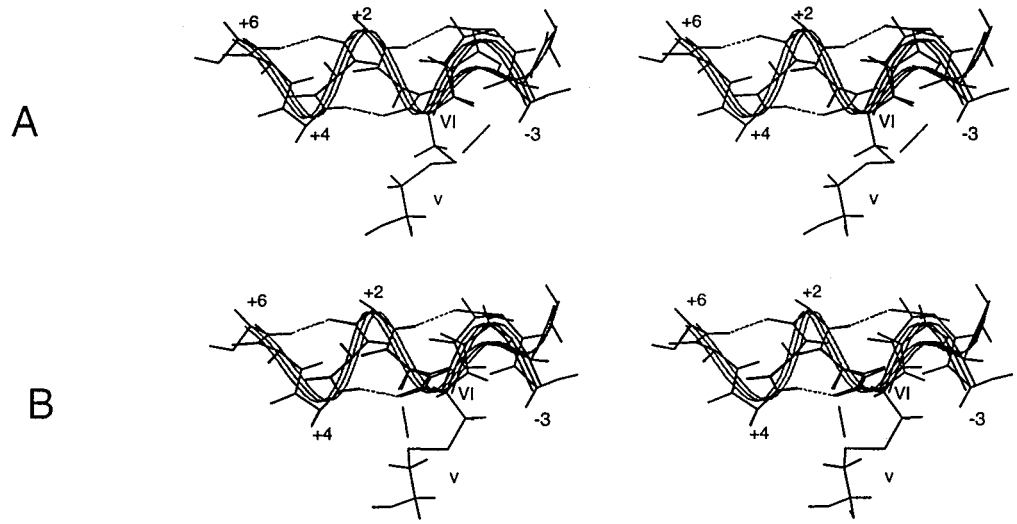

FIGURE 8: Backbone representations of the (A) *S* orientation disulfide bond and helix B as found in the crystal structure of *Tm* Fd (*4*); the α-helix B as shown in shaded lines for backbone atoms, and the loop between the end of helix B and β-sheet A is shown as a solid line. The extension of helix A by one turn in *Pf* relative to *Tm* Fd to the right of Cys48(VI) is shown by shaded lines for the backbone atoms. The strong van der Waals overlap between the Cys(VI) S_γ and Leu45(VI − 3) $C_\alpha H$ and C═O is indicated by a line. (B) Backbone representation of the *R* orientation of the disulfide bridge for the structure of *Tm* Fd with the extended helix B to the right of Cys48(VI) that illustrates the van der Waals overlap between the Cys(V) S_γ and carbonyl of Cys(VI). The residues on helix B are labeled VI ± *i* by their position on helix B relative to the conserved Cys(VI), $i = 1, 2, ...$, with positive and negative *i* indicating the direction of the C- and N-terminus, respectively.

one turn on the C-terminal side relative to *Dg*, *Tm*, and *Tl* Fds, as shown in Figure 8. Because of the differences in length of the *Pf* protein and the other Fds, it is convenient to label the residues on helix B based on *their position relative to the conserved* Cys(VI), with the remainder of the helical residues labeled VI ± *i*, with $i = 1, 2, ...$, where positive and negative *i* reflect the C-terminal and N-terminal positions of the helix, respectively.

Analysis of the Fds (*4*−*7*) with the *S* disulfide orientation shows that the Cys(VI) C_βHs are directed toward the solvent and far (>4 Å) from $C_\alpha H$ of residue VI − 3 (i.e., Leu 45 in *Pf* Fd). The Cys(V) in these same Fds, moreover, places its C_βHs at >3.6 Å from the conserved Val $C_\beta H$ adjacent to the conserved Phe. In contrast, reorientation of the disulfide to the *R* orientation and extending α-helix B by four residues on the C-terminal side moves the Cys(VI) C_βHs to <2.8 Å from both the NH and $C_\alpha H$ of residue VI − 3 (Leu45 in *Pf* Fd). The NOESY map of *Pf* Fd_A^{ox} indeed reveals moderate intensity NOESY cross-peaks between Cys48(VI) C_βHs and the NH and $C_\alpha H$ of Leu45 (not shown; see Supporting Information) as well as between the Cys21(V) C_βHs and the $C_\beta H$ of Val 24 (not shown), confirming that the *R* orientation of the disulfide bond is present in *Pf* Fd_A^{ox}. *We therefore propose that the molecular heterogeneity results from population of the alternate orientations, S and R, for disulfide bond between Cys21(V) and Cys48(VI) at ambient temperatures.*

Notably, there are additional structural consequences of the disulfide bond orientational disorder that propagate widely over the molecular structure. Thus, the line broadening and anomalous temperature gradients for the NH shift on one side of the disulfide form a well-defined hydrogen bond pathway for residues marked in bold in Figure 6 that logically extends to the cluster by virtue of the Cys21(V) NH serving as H-bond donor to the carbonyl of cluster ligand Cys17(III). The other side of the disulfide bond links Cys48(VI) to essentially the complete helix B, but with particularly large environmental differences between the interconverting form for the NHs of Lys50(VI + 2), Ala52(VI + 4) and Glu54(VI + 6). The line broadening of the residues involved in the heterogeneity severely complicates the detection of the NOESY cross-peaks needed to further describe the helix deformation. It is noted, however, that the residues with the severely broadened NH peaks exhibit only very slow exchange with ^2H_2O, indicating that the helix is perturbed but not broken.

Determination of the Disulfide Orientation for the Low- and High-Temperature Form of 4Fe Fd_A^{ox}. It cannot be determined directly at this time whether the long (B) helix of *Pf* Fd_A^{ox} is distorted for the *S* or *R* orientation of the disulfide, or both. However, comparison of the ^1H NMR data for 4Fe Fd_A^{ox} and 4Fe Fd_B^{ox} suggests that the major distortions of helix B *occur primarily for one of the two disulfide orientations* (shown below to be for the *S* orientation). *Thus, it is proposed that one of the two interconverting forms of 4Fe* Fd_A^{ox} *resembles the structure of 4Fe* Fd_B^{ox}, *where the disulfide bond is cleaved and the 13-member helix B is well-formed*. This conclusion is supported by two lines of evidence. On one hand, it has been noted above that the proton signals of precisely those residues of Fd_A^{ox} are *broadened by the disulfide conformational interconversion that also experiences the largest shift changes upon cleavage of the disulfide to form* Fd_B^{ox}. On the other hand, the sign and magnitude of the anomalous NH shift gradient for Fd_A^{ox} show that, as the temperature is elevated, the chemical shifts for these broadened NH peaks for the averaged 4Fe Fd_A^{ox} structure approach those of 4Fe Fd_B^{ox}. Thus, a plot of the temperature gradient for the broadened N_PH signals of 4Fe Fd_A^{ox} in the 10−40 °C range versus the chemical shift difference between Fd_A^{ox} and Fd_B^{ox} at 30 °C, as shown in Figure 9, yields a reasonable correlation, particularly for those residues exhibiting the most positive and most negative gradients.

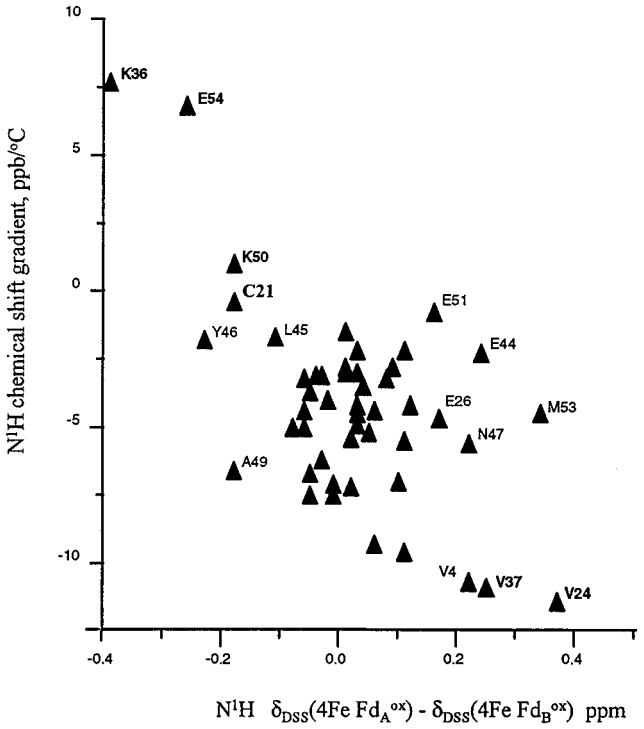

FIGURE 9: Plot of backbone NH chemical shift difference between 4Fe Fd_A^{ox} and 4Fe Fd_B^{ox} (δ_{DSS}(4Fe Fd_A^{ox}) − δ_{DSS}(4Fe Fd_B^{ox})) at 30 °C versus the temperature gradient, $d\delta_{DSS}$(4Fe Fd_A^{ox})/d*T*, in the temperature range 10−40 °C. Residues are labeled where there is a significant shift difference between 4Fe Fd_A^{ox} and 4Fe Fd_B^{ox}. It is noted that the residues at the extremity are those which exhibit the anomalous line broadening due to the dynamic disulfide conformational equilibrium in Fd_A^{ox}.

The ^{1}H NMR spectra in Figure 2 show that the two time-resolved forms of 3Fe Fd_A^{ox} change in population even over the narrow 10−30 °C range, with the isomer Fd_A^{ox}(*S*) (see below) becoming more populated at low temperature. Hence, it could be expected that Fd_A^{ox}(*R*) would become increasingly more populated at elevated temperature where only the averaged structure is detected by NMR. Indeed, as shown for several of the key residues in Figure 5, the gradients in 4Fe Fd_A^{ox} become more "normal" at elevated temperatures, indicating that the system becomes less heterogeneous by converting primarily to one form (*R*) for which the chemical shifts for residues broadened to the heterogeneity approach those of 4Fe Fd_B^{ox}. Moreover, the intensity of the NOESY cross-peaks between Cys48(VI) C_βHs and the Leu45 C_αH (Supporting Information) and Ala49 N_PH (not shown) gains intensity as the temperature is raised, which supports the idea that the species predominating at elevated temperature possesses the *R* disulfide orientation. *The loss of the "anomalous" gradient at high temperature supports that the Fd_A^{ox} converts primarily to the form with "R" chirality about the Cys21(V)−Cys48(VI) disulfide bond under the physiological condition for the organism (T* ∼ 100 °C). Thus the *S* disulfide orientation represents the ground state structure for *Pf* Fd_A^{ox} as in other Fds and allows the assignment of the individual Cys peaks to the *S* and *R* chiralities in the disulfide.

The N_PH temperature gradients in Figure 5 indicated that the N_PH shifts for the *R* disulfide orientation (with the well-formed helix B) are further downfield for Lys50(VI + 2) (donor to CO of Tyr46(VI − 2)) and Glu54(VI + 6) (donor to CO of Lys50(VI + 2)) and further upfield for Ala52(VI + 4) (donor to CO of Cys48(VI)) than for the *S* disulfide orientation. The shift differences are consistent with "stretching" the Lys50(VI + 2) NH and Gln54(VI + 6) NH and "compressing" the Ala52(VI + 4) NH H-bonds for the "bent" helix B with the *S* disulfide compared to the well-formed helix B with the *R* disulfide orientation (see Figure 8).

These conclusions merit three comments. First, the structural differences between the *S* and *R* forms of the disulfide bond in *Pf* Fd are widespread (global) rather than very local. This is in contrast to, for example, the case of the basic pancreatic trypsin inhibitor where alternate orientations are populated for one of the disulfide bonds (which is also the most reducible), and the effect of this heterogeneity is evidenced only for residues highly localized to the vicinity of the disulfide bond (*36*). Second, this global heterogeneity may be the basis for a disordered structure for *Pf* Fd in its cocrystal with its oxidoreductase (*18*). Thus, the heterogeneity, and hence the disorder, may be resolved by using either the Fd_B form (with the reduced disulfide) or an appropriate mutant (e.g., C21A) that precludes forming the disulfide even under aerobic conditions. Third, the described isomers of *Pf* Fd_A^{ox} reveal that the structure in the physiologically relevant temperature range is likely only one of the two species present at ambient temperature and *hence represents an example of a temperature-dependent structure change that is likely relevant to function.*

Influences of Cluster Ligand and Architecture. A comparison between two *Pf* Fd_A forms, each with a disulfide, has to consider both changes in the equilibrium between the proposed disulfide conformations and changes in the structure of one or both of the components. Changes in the population of the *S* and *R* disulfide orientation, however, should induce shift changes in a well-defined pattern as reflected in either the ^{1}H chemical shift gradient or the shift difference between 4Fe Fd_A^{ox} and 4Fe Fd_B^{ox}. The NOESY pattern for both 3Fe and 4Fe D14C forms of Fd_A^{ox} are essentially the same as for 4Fe Fd_A^{ox}; however, the shifts for the majority of residues are altered, as shown in Figure 4A,B, indicating small but widespread accommodation to the cluster perturbations which are generally much larger upon removing an iron than substituting Cys for Asp14. Interestingly, for Fd_A^{ox} the shifts for the NH of heterogeneity-sensitive Cys21, Val24, Lys36, Val37, and Lys50 are not significantly changed upon substitution of Asp14 by Cys or by deleting an iron, indicating that the relative stability of the *S*- and *R*-conformations of the disulfide is insensitive to the cluster architecture or cluster ligand. However, more detailed comparisons among these derivatives will require the development of robust molecular models for both forms of the protein with the disulfide bridge.

For both 3Fe and 4Fe D14C Fd_A^{ox}, significant shift changes are observed for residues whose backbones are expected to be relatively close to the cluster, e.g., Ser19, Lys32, and Met53, all of which are moderately relaxed by the cluster and potentially exhibit variable dipolar shifts that complicate structural interpretation at this time. However, it is unlikely that all changes are due to dipolar shifts. For example, the large perturbations to Gln8 and Leu20 NHs can be rationalized by the fact that the structures of single cubane cluster Fds (*4*−*9*) predict a van der Waals contact between Gln8 C_βH and the carbonyl of Cys11 and between Leu20 C_βH and the carbonyl of Ile16. It is reasonable to

expect that changing the ligand at position 14, or eliminating it entirely, would alter the orientation of the loop between Cys11 and Cys17.

Role of the Sequence Extension in Pf Fd. Pf Fd, like *Tl* and *Tm* Fds, differs from the Fds from mesophiles by expanding β-sheet A to include several more backbone hydrogen bonds to a turn (*4*) or third strand (*6*). This common theme among these hyperthermostable Fds argues for an important role of this expansion in enhancing their thermostability. On the other hand, the role of the six- to seven-residue extension in the *Pf* Fd and its effect on the thermostability in this protein are less clear. While the growth temperatures of *Tm* (80 °C) and *Pf* (100 °C) differ by about 20 °C, there is evidence that their Fds are comparably thermostable (*17*, *37*). Hence it does not appear likely that the extensions of β-sheet A and α-helix B in *Pf* Fd relative to *Tl* and *Tm* Fds are present primarily to enhance the thermostability of the former over the latter. We have concluded above, however, that helix B is not well formed in the presence of the disulfide bond, with the C-terminal portion distorted in some fashion for the *S* orientation. Hence, it can be argued that the disulfide bond destabilizes the 13-member helix B, or perhaps more relevantly, a "normal", well-formed 13-member helix B *destabilizes the disulfide bond* in *Pf* Fd, making it more reducible than a similar bond in *Tm* or *Tl* Fds. Therefore the extension of helix B at its N-terminus and elongation of β-sheet A at both C- and N-termini likely result in a less favorable relative orientation of Cys21(V) and Cys48(VI) for forming the disulfide bond. These arguments lead to the conclusion that, while *Pf* and *Tm* Fds with intact disulfide bonds may have comparable thermostability, cleaving this bond should destabilize *Tm* Fd more than *Pf* Fd. Since the standard nine-member helix B in the other hyperthermostable *Tm* and *Tl* Fds (*4*−*6*) leads to a disulfide bond exclusively in the *S* orientation that is not reducible by dithionite, a reasonable deduction is that *the six- to seven-residue extension of Pf relative to Tm or Tl Fds has at least one of the roles to destabilize the disulfide bond*. It has been noted in other proteins with multiple disulfide bonds that the tendency to populate the higher energy *R* chirality (*36*) correlates with the reducibility of the disulfide bond (*38*). The physiological significance, if any, for this in *Pf* Fd is unknown at present.

ACKNOWLEDGMENT

The authors are indebted to Dr. C. M. Gorst for useful discussion and experimental assistance.

SUPPORTING INFORMATION AVAILABLE

Four tables (chemical shifts for 4Fe Fd_A^{ox}, 4Fe Fd_B^{ox}, 3Fe Fd_A^{ox}, and 4Fe Fd_B^{ox}), and five figures ($^1H-^{15}N$ HSQC spectra for 4Fe Fd_A^{ox} as a function of temperature, $^1H-^{15}N$ HSQC spectrum of a mixture of 4Fd Fd_A^{ox} and 4Fe Fd_B^{ox}, TOCSY spectrum for Cys 48 of 4Fe Fd_A^{ox} and 4Fe Fd_B^{ox}, NOESY contacts between Cys48 and Leu45 in 4Fe Fd_A^{ox}, saturation transfer spectra for 4Fe Fd_A^{ox}). This material is available free of charge via the Internet at http://pubs.acs.org.

REFERENCES

1. Cammack, R. (1992) *Adv. Inorg. Chem. 38*, 281−322.
2. Johnson, M. K. (1994) in *Encyclopedia of Inorganic Chemistry* (King, R. B., Ed.) pp 1896−1915, John Wiley, New York.
3. Beinert, H., Holm, R. H., and Münck, E. (1997) *Science 277*, 653−659.
4. Macedo-Ribeiro, S., Darimont, B., Sterner, R., and Huber, R. (1996) *Structure 4*, 1291−1301.
5. Sticht, H., Wildegger, G., Dentrop, D., Darimont, B., Sterner, R., and Rösch, P. (1996) *Eur. J. Biochem. 237*, 726−735.
6. Wang, P.-L., Donaire, A., Zhou, Z. H., Adams, M. W. W., and La Mar, G. (1996) *Biochemistry 35*, 11319−11328.
7. Kissinger, C. R., Sieker, L. C., Adman, E. T., and Jensen, L. H. (1991) *J. Mol. Biol. 219*, 693−715.
8. Sery, A., Housset, D., Serre, L., Bonicel, J., Hatchikian, C., Frey, F., and Roth, M. (1994) *Biochemistry 33*, 15408−15417.
9. Fukuyama, K., Matsubara, H., Tsukihara, T., and Katsube, Y. (1989) *J. Mol. Biol. 210*, 383−398.
10. Calzolai, L., Gorst, C. M., Zhou, Z. H., Teng, Q., Adams, M. W. W., and La Mar, G. N. (1995) *Biochemistry 34*, 11373−11384.
11. Conover, R. C., Kowal, A. T., Fu, W., Park, J.-B., Aono, S., Adams, M. W. W., and Johnson, M. K. (1990) *J. Biol. Chem. 265*, 8533−8541.
12. Calzolai, L., Zhou, Z. H., Adams, M. W. W., and La Mar, G. N. (1996) *J. Am. Chem. Soc. 118*, 2513−2514.
13. Donaire, A., Gorst, C. M., Zhou, Z. H., Adams, M. W. W. W., and La Mar, G. N. (1994) *J. Am. Chem. Soc. 116*, 6841−6849.
14. Gorst, C. M., Zhou, Z. H., Ma, K., Teng, Q., Howard, J. B., Adams, M. W. W., and La Mar, G. (1995) *Biochemistry 34*, 8788−8795.
15. Calzolai, L., Gorst, C. M., Bren, K. L., Zhou, Z. H., Adams, M. W. W., and La Mar, G. N. (1997) *J. Am. Chem. Soc. 119*, 9341−9350.
16. Busse, S. C., La Mar, G. N., Yu, L. P., Howard, J. B., Smith, E. T., Zhou, Z. H., and Adams, M. W. W. (1992) *Biochemistry 31*, 11952−11962.
17. Teng, Q., Zhou, Z. H., Smith, E. T., Busse, S. C., Howard, J. B., Adams, M. W. W., and La Mar, G. N. (1994) *Biochemistry 33*, 6316−6326.
18. Yu, L., Faham, S., Roy, R., Adams, M. W. W., and Rees, D. C. (1999) *J. Mol. Biol. 286*, 899−914.
19. Gorst, C. M., Yeh, Y.-H., Teng, Q., Calzolai, L., Zhou, Z. H., Adams, M. W. W., and La Mar, G. (1995b) *Biochemistry 34*, 600−611.
20. Aono, S., Bryant, F. O., and Adams, M. W. W. (1989) *J. Bacteriol. 171*, 3433−3439.
21. Blake, P. R., Park, J. B., Bryant, F. O., Aono, S., Magnuson, J. K., Eccleston, E., Howard, J. B., Summers, M. F., and Adams, M. W. W. (1991) *Biochemistry 30*, 10885−10891.
22. Sambrook, J., Fritsch, E. F., and Maniatis, T. (1989) *Molecular Cloning: A Laboratory Manual Volumes 1−3*, 2nd ed., Cold Spring Harbor Laboratory Press, Plainview, NY.
23. Heltzel, A., Smith, E. T., Zhou, Z. H., Blamey, J. M., and Adams M. W. W. (1994) *J. Bacteriol. 176*, 4790−4793.
24. Venters, R. A., Calderone, T. L., Spicer, L. D., and Fierke, C. A. (1991) *Biochemistry 30*, 4491−4494.
25. Plateaue, P., and Gueron, M. (1982) *J. Am. Chem. Soc. 104*, 7321−7311.
26. Bax, A., and Davis, D. G. (1985) *J. Magn. Reson. 65*, 355−360.
27. Brown, S. C., Weber, P. L., and Müller, L. (1988) *J. Magn. Reson. 77*, 166−169.
28. Jeener, J., Meier, B. H., Bachmann, P., and Ernst, R. R. (1979) *J. Chem. Phys. 71*, 4546−4553.
29. Bax, A., Ikura, M., Kay, L. E., Torchia, D. E., and Tshudin, R. (1990) *J. Magn. Reson. 86*, 304−318.
30. Wüthrich, K. (1986) *NMR of Proteins and Nucleic Acids*, Wiley & Sons, New York.

31. Anderson, N. H., Neidigh, J. W., Harris, S. M., Lee, G. M., Liu, Z., and Tong, H. (1997) *J. Am. Chem. Soc. 119*, 8547−8561.
32. Baxter, N. J., and Williamson, M. D. (1997) *J. Biomol. NMR 9*, 359−369.
33. Wishart, D. S., Sykes, B. D., and Richards, F. M. (1991) *J. Mol. Biol. 222*, 311−333.
34. Richardson, J. S. (1981) *Adv. Protein Chem. 34*, 167−330.
35. Srinivasan, N., Sowbhamini, R., Ramakrishnan, C., and Balaram, P. (1990) *Int. J. Protein Res. 36*, 147−155.
36. Otting, G., Liepinsh, E., and Wüthrich, K. (1993) *Biochemistry 32*, 3571−3582.
37. Pfeil, W., Gesierich, U., Kleemann, G. R., and Steiner, R. (1997) *J. Mol. Biol. 272*, 591−596.
38. Kress, L. F., and Laskowski, M., Sr. (1967) *J. Biol. Chem. 242*, 4925−4929.

BI990241N